A&A, 694, A37 (2025)
https://doi.org/10.1051/0004-6361/202451775

Astronomy & Astrophysics

Discovery of polarized X-ray emission from the accreting millisecond pulsar SRGA J144459.2–604207

Alessandro Papitto[1,⋆], Alessandro Di Marco[2], Juri Poutanen[3,4], Tuomo Salmi[5,6], Giulia Illiano[1,7,8], Fabio La Monaca[2,7,8], Filippo Ambrosino[1], Anna Bobrikova[3], Maria Cristina Baglio[9], Caterina Ballocco[1,8], Luciano Burderi[10,11], Sergio Campana[9], Francesco Coti Zelati[12,13], Tiziana Di Salvo[14], Riccardo La Placa[1], Vladislav Loktev[3], Sinan Long[15], Christian Malacaria[1], Arianna Miraval Zanon[16], Mason Ng[17], Maura Pilia[18], Andrea Sanna[11], Luigi Stella[1], Tod Strohmayer[19,20], and Silvia Zane[15]

[1] INAF Osservatorio Astronomico di Roma, Via Frascati 33, 00078 Monte Porzio Catone, (RM), Italy
[2] INAF Istituto di Astrofisica e Planetologia Spaziali, Via del Fosso del Cavaliere 100, 00133 Roma, Italy
[3] Department of Physics and Astronomy, 20014 University of Turku, Finland
[4] Space Research Institute, Russian Academy of Sciences, Profsoyuznaya 84/32, 117997 Moscow, Russia
[5] Anton Pannekoek Institute for Astronomy, University of Amsterdam, Science Park 904, 1098 XH Amsterdam, The Netherlands
[6] Department of Physics, PO Box 64, 00014 University of Helsinki, Finland
[7] Dipartimento di Fisica, Università degli Studi di Roma “Tor Vergata”, Via della Ricerca Scientifica 1, 00133 Roma, Italy
[8] Dipartimento di Fisica, Università degli Studi di Roma “La Sapienza”, Piazzale Aldo Moro 5, 00185 Roma, Italy
[9] INAF Osservatorio Astronomico di Brera, Via E. Bianchi 46, 23807 Merate, (LC), Italy
[10] INAF/IASF Palermo, Via Ugo La Malfa 153, 90146 Palermo, Italy
[11] Dipartimento di Fisica, Università degli Studi di Cagliari, SP Monserrato-Sestu, KM 0.7, Monserrato 09042, Italy
[12] Institute of Space Sciences (ICE, CSIC), Campus UAB, Carrer de Can Magrans s/n, 08193 Barcelona, Spain
[13] Institut d’Estudis Espacials de Catalunya (IEEC), 08860 Castelldefels, (Barcelona), Spain
[14] Dipartimento di Fisica e Chimica – Emilio Segrè, Università di Palermo, Via Archirafi 36, 90123 Palermo, Italy
[15] Mullard Space Science Laboratory, University College London, Holmbury St Mary, Dorking, Surrey RH5 6NT, UK
[16] ASI – Agenzia Spaziale Italiana, Via del Politecnico snc, 00133 Rome, (RM), Italy
[17] MIT Kavli Institute for Astrophysics and Space Research, Massachusetts Institute of Technology, Cambridge, MA 02139, USA
[18] INAF Osservatorio Astronomico di Cagliari, Via della Scienza 5, 09047 Selargius, (CA), Italy
[19] Astrophysics Science Division, NASA Goddard Space Flight Center, Greenbelt, MD 20771, USA
[20] Joint Space-Science Institute, NASA Goddard Space Flight Center, Greenbelt, MD 20771, USA

Received 2 August 2024 / Accepted 7 December 2024

ABSTRACT

We report the discovery of polarized X-ray emission from an accreting millisecond pulsar. During a 10-day-long coverage of the February 2024 outburst of SRGA J144459.2–604207, the Imaging X-ray Polarimetry Explorer (IXPE) detected an average polarization degree of the 2–8 keV emission of 2.3% ± 0.4% at an angle of 59° ± 6° (east of north; the uncertainties quoted are at the 1σ confidence level). The polarized signal shows a significant energy dependence with a degree of 4.0% ± 0.5% between 3 and 6 keV and <1.5% (90% c.l.) in the 2–3 keV range. We used NICER, XMM–Newton, and NuSTAR observations to obtain an accurate pulse-timing solution and to perform a phase-resolved polarimetric analysis of IXPE data. We did not detect any significant variability in the Stokes parameters Q and U with the spin and orbital phases. We used the relativistic rotating-vector model to show that a moderately fan-beam emission from two point-like spots at low magnetic obliquity ($\simeq 10^\circ$) is compatible with the observed pulse profile and polarization properties. IXPE also detected 52 type I X-ray bursts whose recurrence time $\Delta t_{\rm rec}$ increased from 2 to 8 h as a function of the observed count rate C as $\Delta t_{\rm rec} \propto C^{-0.8}$. We stacked the emission observed during all the bursts and obtained an upper limit on the polarization degree of 8.5% (90% c.l.).

Key words. magnetic fields – polarization – methods: observational – stars: neutron – pulsars: individual: SRGA J144459.2–604207 – X-rays: binaries

1. Introduction

The simultaneous measurement of the mass M and the equatorial radius $R_{\rm eq}$ of a few neutron stars (NSs) is of paramount importance for constraining the equation of state of ultradense matter because of its one-to-one mapping to the NS mass–radius dependence (Lattimer & Prakash 2016; Özel & Freire 2016; Baym et al. 2018). Relativistic effects bend the light trajectory and modify the energy of the photons that are emitted by hot spots on the surface of millisecond pulsars (MSPs; see, e.g., Watts et al. 2016, and references therein). As a result, the modeling of the X-ray pulse profiles of MSPs is one of the most powerful techniques for obtaining the desired information on M and $R_{\rm eq}$ (Poutanen & Gierliński 2003; Miller & Lamb 2016). The pulse shape also depends on several geometrical parameters (e.g., the binary inclination i, the spot colatitude θ, and its angular size ρ) as well as spectral parameters (e.g., the angular pattern of the emitted radiation; see, e.g., Poutanen & Beloborodov

---

[⋆] Corresponding author; `alessandro.papitto@inaf.it`

2006 and Section 3.2.3). Breaking this degeneracy with X-ray spectral-timing data requires a very large number of counts (Lo et al. 2013; Miller & Lamb 2015). A few megasecond-long observations of rotation-powered MSPs with the Neutron Star Interior Composition Explorer Mission (NICER) met this requirement and led to constraints on M and $R_{\rm eq}$ with a relative uncertainty of ~10% for three of them (Riley et al. 2019, 2021; Miller et al. 2019, 2021; Choudhury et al. 2024; Dittmann et al. 2024; Salmi et al. 2024; Vinciguerra et al. 2024).

Accreting MSPs (AMSPs; Patruno & Watts 2021; Di Salvo & Sanna 2022) represent an intriguing alternative. During accretion outbursts, they attain an X-ray luminosity of $L_X \simeq 10^{36}$–10^{37} erg s^{-1}, which is 5–6 orders of magnitude brighter than rotation-powered MSPs. The degeneracy between M and $R_{\rm eq}$ and the geometrical and spectral parameters of the spot (see, e.g., Viironen & Poutanen 2004) hampered obtaining meaningful constraints from the data taken with the Rossi X-ray Timing Explorer, for example ($M = 1.2$–$1.6\,M_\odot$, $R_{\rm eq} = 6$–13 km by Poutanen & Gierliński 2003; $M = 0.8$–$1.7\,M_\odot$, $R_{\rm eq} = 5$–13 km by Morsink & Leahy 2011). However, Salmi et al. (2018) showed that if i and θ were known a priori with an accuracy of a few degrees, these data would have allowed measurements with a relative uncertainty comparable to or slightly smaller than that for rotation-powered MSPs.

X-ray polarimetry might provide key information on the geometrical parameters of the spots. Soft photons from the NS surface are Compton upscattered by hot electrons in the accretion shock (Poutanen & Gierliński 2003) achieving a polarization degree (PD) from a few percent up to 10–20% (Nagirner & Poutanen 1994; Viironen & Poutanen 2004; Salmi et al. 2021; Bobrikova et al. 2023). For the magnetic field strength of AMSPs (10^8–10^9 G), the typical energy of X-ray photons is higher by several orders of magnitude than the fundamental cyclotron energy ($\simeq$1–10 eV), and scattering is not affected by the magnetic field. As a result of azimuthal symmetry, the polarization vector of the X-rays emitted from the accretion shock is expected to lie either in the meridional plane, which is formed by the photon momentum and the normal to the surface, or perpendicular to it (Viironen & Poutanen 2004; Poutanen 2020). As the NS rotates, the polarization angle (PA) should thus swing as a function of the pulsar spin phase in accordance with the rotating-vector model (RVM; Radhakrishnan & Cooke 1969; Meszaros et al. 1988). In AMSPs, the relativistic motion of the emission regions causes an additional rotation of the polarization plane (Poutanen 2020); the oblate shape of a fast-rotating NS also has to be accounted for Loktev et al. (2020).

We report the discovery of polarized X-ray emission from the AMSP SRGA J144459.2−604207 (SRGA J1444 in the following) by the Imaging X-ray Polarimetry Explorer (IXPE; Weisskopf et al. 2022) in the context of a campaign that also included NICER, X-ray Multi-Mirror Mission (XMM–Newton), and Nuclear Spectroscopic Telescope Array (NuSTAR) observations. Discovered in outburst on 2024 February 21 by the *Mikhail Pavlinsky* ART-XC telescope on board the Spectrum-Roentgen-Gamma observatory (SRG, Molkov et al. 2024) at a relatively bright 4–12 keV X-ray flux of 2×10^{-9} erg s^{-1} cm^{-2} (see Fig. 1), SRGA J1444 showed coherent pulsations at 447.9 Hz that were first detected by NICER from an NS on a 5.2 h orbit around a donor with a mass in the range of 0.2–0.7 $M_\odot$ (Ng et al. 2024). SRGA J1444 also showed type I X-ray bursts (Mariani et al. 2024) quite regularly, with a recurrence time that increased from 1.6 to 2.2 h with decreasing X-ray flux (Molkov et al. 2024). No optical counterpart could be identified (Baglio et al. 2024) at the most accurate X-ray position obtained with High Resolution Camera observations on board the Chandra X-ray observatory (CXO, Illiano et al. 2024), most likely due to the extinction of $A_V \simeq 7$ mag (estimated[1] using the maps of Doroshenko 2024, at a distance of 8 kpc) in that direction. Russell et al. (2024) reported a radio counterpart with a flux density of ~200 μJy at 5.5 GHz and a flat spectral shape, consistent with a compact jet or discrete ejecta.

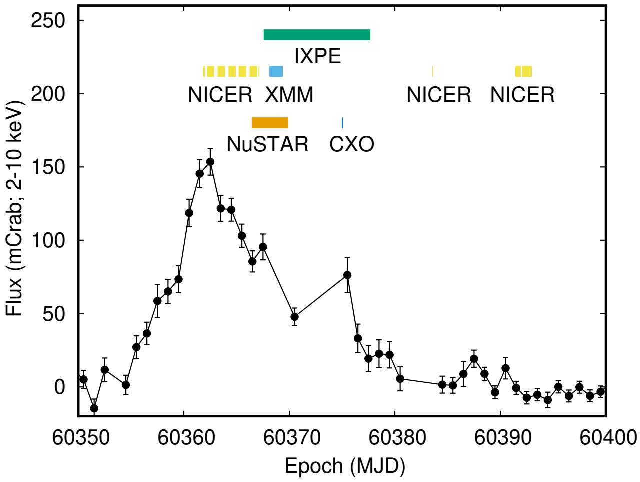

Fig. 1. Light curve of the 2024 outburst of SRGA J1444 observed by the Monitor of All-sky X-ray Image (MAXI, Matsuoka et al. 2009). We converted 2–20 keV observed count rates into 2–10 keV flux values assuming that the spectrum is described by a power law with a photon index $\Gamma = 1.9$ absorbed by an equivalent hydrogen column of $N_{\rm H} = 2.9\times10^{22}$ cm^{-2} (Ng et al. 2024). The horizontal bars indicate the time intervals covered by observations of the instruments.

This paper is organized as follows. Section 2 details the analysis of the different X-ray datasets we considered. Section 3 presents the properties of the persistent[2] X-ray emission. The measurement of the polarized emission is presented in Sect. 3.1.1, and it is interpreted in Sect. 3.1.2. Section 3.2.1 reports the pulsar timing solution obtained from the analysis of the coherent X-ray pulsations observed by the various instruments involved in this analysis, Sect. 3.2.2 reports the observed phase-resolved variability in the polarized emission, and Sect. 3.2.3 reports its modeling. Section 4 outlines the recurrence properties of the type I X-ray bursts detected by IXPE, Sect. 4.1 describes its the X-ray polarization, and Sect. 4.2 reports the physical implications. The main results of this paper are summarized in Sect. 5.

2. Observations

Table 1 lists the observations we analyzed using the HEASoft package version 6.33.2. IXPE started observing SRGA J1444 less than a week after the first detection of the source in response to the trigger of the general observer (GO) program 03250101 (PI: A. Papitto). Observations lasted ~10 d with visibility gaps. The duty cycle exceeded 60%. We used the `pcube` algorithm in the `xpbin` tool of the IXPEOBSSIM package version 30.6.4 (Baldini et al. 2022), along with the IXPE calibration database (CALDB) released on 2024 February 28, to extract polarimetric

---

[1] See the tool available at http://astro.uni-tuebingen.de/nh3d/nhtool

[2] Here, persistent refers to the accretion-powered X-ray emission seen during the outburst, as opposed to the burst emission.

Table 1. Observations.

Observatory	Obs. ID	Start date (MJD)	End date (MJD)	Instrument	Exposure (s)	Energy band (keV)
IXPE	03250101	60 367.556	60 377.676	DU1	552 930	2–8
				DU2	553 541	
				DU3	554 066	
NICER	620419	60 361.831	60 363.908	XTI	9536	0.3–10
	663908	60 364.219	60 392.971		24 805	
NuSTAR	80901307002	60 366.459	60 369.883	FPMA	157 675	3–79
				FPMB	157 440	
XMM–Newton	0923171501	60 368.102	60 369.376	EPIC-pn	110 077	0.3–10

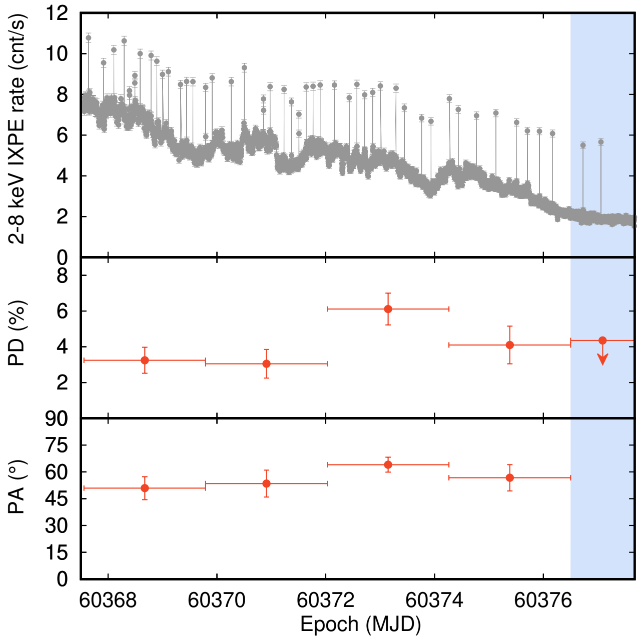

Fig. 2. IXPE 2–8 keV light curve in 200 s time bins (top panel). Type I X-ray bursts are easily recognized. PD (middle panel) and PA (bottom panel) of the total (i.e., persistent and bursting) emission measured in the 3–6 keV band and evaluated over ~2 d long intervals. The blue shaded region indicates the interval after the increase in the pulse amplitude that was observed at MJD 60 376.5, in which a 90% c.l. upper limit on the PD is reported.

information using the formalism from Kislat et al. (2015). We selected source photons from a circular region with a radius of 100″ centered at the source position. We used the unweighted analysis implemented in IXPEOBSSIM (Di Marco et al. 2022) to measure the Stokes parameters (I, Q, U). Figure 2 shows the 2–8 keV IXPE count rate, the polarization degree PD = $\sqrt{q^2 + u^2}$, and the angle PA = $\frac{1}{2}$ arctan(u/q) measured in the 3–6 keV band, where a significant polarization is detected (see Sect. 3.1.1 and Fig. 4). Here, $q = Q/I$ and $u = U/I$. As the source count rate is relatively high (~2–8 count s^{-1}), the background contributes 5% at most to the total rate, and we did not subtract it following the recommendation of Di Marco et al. (2023). For the IXPE spectral analysis, we used the response matrices 20240101_ALPHA075 present in the CALDB, computed ancillary response files using `ixpecalcarf` by weighting the Stokes parameters following the analysis presented by Di Marco et al. (2022), and binned the I spectra to have 30 counts per bin at least. To ensure that the statistics were high enough for a spectropolarimetric analysis, we binned data to a constant resolution of 200 eV.

Ng et al. (2024) reported the analysis of NICER observations during the first three days of the outburst using publicly available data. We also included data taken afterward in the GO program ID 663908 (PI: Papitto). Visibility constraints and high background prevented NICER from collecting data simultaneously with the IXPE (see Fig. 1). The monitoring briefly resumed on 2024 March 14 and more regularly after March 21, when the source count rate had already decreased to close to the background value. We reduced the observations using calibration version XTI20240206 and the same filtering criteria as were adopted by Ng et al. (2024), retaining photons with an energy ranging between 0.3 and 10 keV for a pulse-timing analysis.

The European Photon Imaging Camera (EPIC) pn-CCD camera on board XMM–Newton observed SRGA J1444 uninterruptedly for ~110 ks. We retained 0.3–10 keV source photons extracted from a 21-pixel-wide stripe (equivalent to 86.″1) around the position of the pulsar to perform a pulse-timing analysis.

NuSTAR provided the longest overlap with IXPE data starting on 2024 February 26. We reduced the data using the calibration version INDX20240325, with the fine-clock correction file version 192. A circular region with a wide radius of 140″ was adopted to extract source photons in the 3–79 keV band.

The times of arrival of the photons recorded by all the instruments were transformed into the inertial reference frame centered at the Solar System barycenter using the Chandra coordinates reported by Illiano et al. (2024), RA = 14$^{\rm h}$ 44$^{\rm m}$ 58.$^{\rm s}$94, Dec = −60° 41′ 55.″3 (J2000) and the DE 405 ephemeris. We detected 52, 5, 13, and 23 type I X-ray bursts during IXPE, NICER, XMM–Newton, and NuSTAR exposures, respectively. When we analyzed the persistent emission, we discarded intervals between 5 s before and 60 s after the onset of each burst.

3. Persistent X-ray emission

3.1. Phase-averaged emission

3.1.1. Average polarization

Figure 3 shows the average normalized Stokes parameters observed during the peristent emission by the three IXPE detector units (DUs). The average Stokes parameters are $q = -1.1\% \pm 0.4\%$ and $u = 2.0\% \pm 0.4\%$, which translate into an average PD of 2.3% ± 0.4%, and an angle of PA 59° ± 6° (measured east of north; see Fig. 3). The errors are quoted at the 1σ confidence level (c.l.) unless differently specified. The probability of detecting these values of the normalized Stokes parameters from noise fluctuations is 1.1×10^{-7} (corresponding to a 5.3σ c.l.).

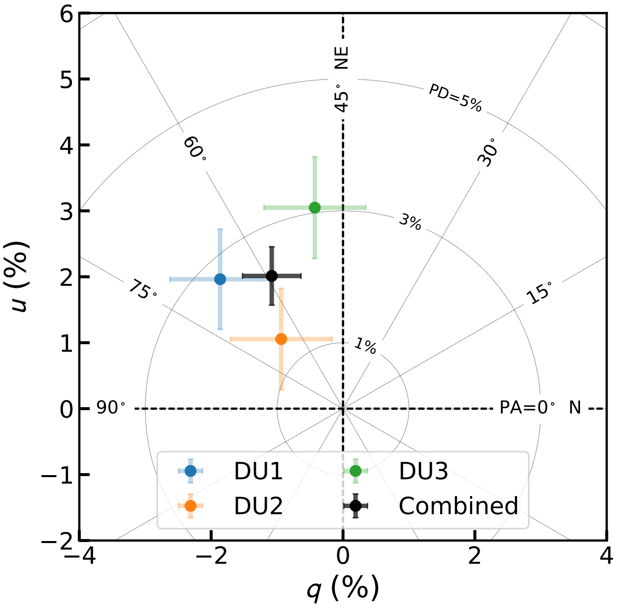

Fig. 3. Average normalized Stokes parameters observed during the 2–8 keV persistent emission for the single IXPE DUs and for the sum.

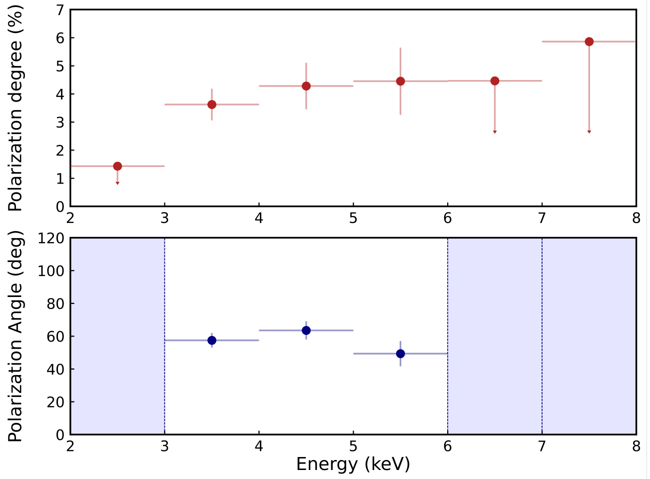

Fig. 4. Polarization degree (top) and PA (bottom) as a function of energy. Above 6 keV, the polarization is compatible with zero, and we report upper limits at the 90% c.l., while the PA is unconstrained.

Figure 4 shows the results of an energy-resolved analysis. Polarized emission is detected at the highest statistical significance in the 3–6 keV energy range with an average $\mathrm{PD}_{3-6} = 4.0\% \pm 0.5\%$ and $\mathrm{PA}_{3-6} = 57° \pm 3°$. Between 2 and 3 keV, the PD is not significant (0.7% ± 0.6%), with an upper limit at the 90% c.l. of $\mathrm{PD}_{2-3} < 1.5\%$. Above 6 keV, the 5% upper limit on the PD becomes larger than both PD_{3-6} and the minimum detectable polarization at 99% c.l. in the 3–6 keV band ($\mathrm{MDP}_{99} = 1.4\%$). We did not detect any significant variation or rotation of the 3–6 keV polarization vector over 2 d long intervals, even though the PD slightly increased halfway through the observation (see the bottom panels of Fig. 2). We checked that no significant variation occurred in the spectral parameters in the time interval characterized by a slightly larger PD compared to the emission observed elsewhere.

Similar to Ng et al. (2024), we used the sum of a blackbody (`bbodyrad` in XSPEC) and thermal Comptonization (`nthcomp`) to satisfactorily model (χ^2 = 483.9 for 441 d.o.f.) the 2–8 keV IXPE energy spectrum. We modeled absorption with the Tuebingen-Boulder model (Wilms et al. 2000) with the absorption column fixed to $N_\mathrm{H} = 2.9 \times 10^{22}\,\mathrm{cm}^{-2}$ and quote the uncertainties on the spectral parameters at the 90% c.l. The thermal component has a temperature of $kT_\mathrm{bb} = 0.52 \pm 0.01$ keV and an apparent size of $R_\mathrm{bb} = (14.0 \pm 0.5)\, d_8$ km, where d_8 is the distance to the source in units of 8 kpc. Comptonization is described by an asymptotic power law with index $\Gamma = 1.70 \pm 0.03$ and a soft-photon input with a temperature <0.15 keV. The electron temperature was fixed at a value beyond the IXPE bandpass kT_e = 15 keV. The Comptonization component accounts for ~95% of the 2–8 keV observed flux of $(5.6 \pm 0.1) \times 10^{-10}\,\mathrm{erg\,s^{-1}\,cm^{-2}}$. The spectral analysis of the NICER observation (Obs. ID 6639080103) performed ~12 h before the start of the IXPE coverage indicates a smaller blackbody ($kT_\mathrm{bb} = 0.68 \pm 0.05$ keV; $R_\mathrm{bb} = (5.7 \pm 1.0)\, d_8$ km) and a steeper slope of the Comptonized emission ($\Gamma = 1.90 \pm 0.01$).

The decrease in the PD below 3 keV, that is, in the energy range where the soft thermal component contributes the most, motivated us to perform a spectropolarimetric analysis. By fitting the spectra of the three Stokes parameters with a constant polarization component to multiply the model presented above, `tbabs*(bbodyrad+nthcomp)*polconst`, gave PD = 2.6% ± 0.5% and PA = 59° ± 6° with a χ^2/d.o.f. of 340/257, which is compatible with the `pcube` results. By using a separate constant polarization for the two spectral components, we slightly improved the fit χ^2/d.o.f. = 328/255 with a `bbodyrad` component polarized with the PD = 8% ± 5% at PA = −43° ± 19° and the `nthcomp` with the PD = 4.6% ± 1.1% and PA = 55° ± 7°.

3.1.2. Interpretation

For the first time, IXPE observations of SRGA J1444 allowed us to significantly detect polarization from an AMSP with an average 2–8 keV degree of 2.3% ± 0.4%. This value increases to 4.0% ± 0.5% when the analysis is restricted to the 3–6 keV energy band. Comptonization by hot ($kT_\mathrm{e} \sim$ 20–60 keV) electrons in slabs of moderate optical depth ($\tau \approx 1$–2) located above hot spots ($kT_\mathrm{bb} \sim$ 1 keV) on the NS surface accounts for more than 90% of the emission in the IXPE bandpass of AMSPs such as SRGA J1444 (Poutanen 2006) and represents the most natural explanation of the polarization we detected. Values of the PD as high as 10–20% were predicted by modeling the scattering in Thomson approximation (Viironen & Poutanen 2004; Salmi et al. 2021). However, the actual degree of polarization is a function of the physical properties of the scattering medium (Nagirner & Poutanen 1994). Recently, Bobrikova et al. (2023) applied the formalism for Compton scattering in a hot slab (Nagirner & Poutanen 1993; Poutanen & Svensson 1996) to describe the Stokes parameters as a function of energy and angle in terms of the electron temperature and optical depth of the slab and the seed photon temperature. They found values of the PD of a few percent at most, which decreased to values that cannot be detected by IXPE at high (>50 keV) electron temperatures. They concluded that chances for IXPE to detect polarization from an AMSP significantly increased for systems with a higher optical depth ($\tau > 2$) and lower electron temperature ($kT_\mathrm{e} <$ 30 keV). Molkov et al. (2024) fit the 4–30 keV ART-XC spectrum with Comptonization from a medium with $kT_\mathrm{e} \sim$ 25 keV and $\tau \sim 3.2$ (evaluated from the photon index of $\Gamma = 1.8$ as in, e.g., Lightman & Zdziarski 1987). Preliminary fitting of the 3–79 keV NuSTAR spectrum (Malacaria et al., in prep.) suggested an even lower temperature ($kT_\mathrm{e} = 10.9^{+0.2}_{-0.1}$ keV) and

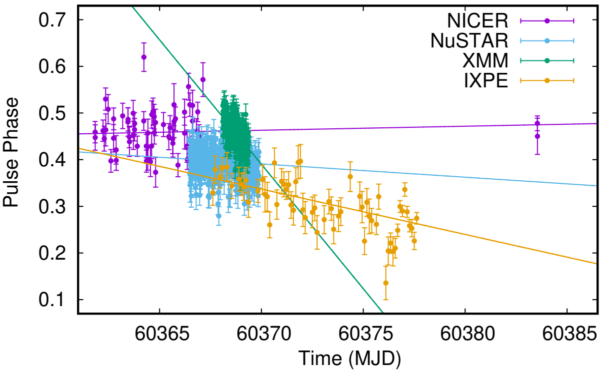

Fig. 5. Pulse phase computed over the first harmonic of the pulses observed by NICER (magenta), NuSTAR (light blue), XMM–Newton (green), and IXPE (yellow) by folding 500 s long intervals (5 ks for IXPE) around $\nu_{\rm fold}$ (see Table 2) with a reference epoch 60 361.8 MJD. The solid lines mark the best-fit linear trends.

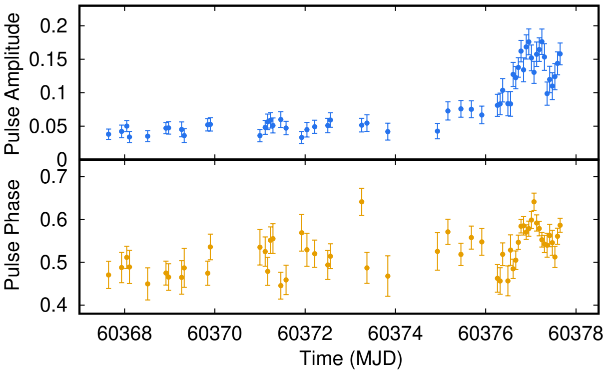

Fig. 6. Pulse fractional amplitude and phase of the first harmonic component used to model the pulse profile obtained by folding IXPE data into 5 ks long interval around the timing solution reported in the rightmost column of Table 2.

higher optical depth ($\Gamma = 2.2 \pm 0.1$, $\tau = 4.0 \pm 0.3$). In the framework developed by Bobrikova et al. (2023), SRGA J1444 may thus present favorable spectral conditions to produce a relatively high degree of X-ray polarization compared to other AMSPs that might even show lower values. In addition, Bobrikova et al. (2023) showed that the observed polarization degree increased when an observer mostly sees the spot at high angles (i.e., $|i - \theta|$ close to 90°). This configuration is supported by the results presented in Sect. 3.2.2.

We detected a significant decrease in the PD below 3 keV. In the IXPE bandpass, the non-upscattered blackbody emission contributes most to the total observed flux in this energy band. These photons are not expected to be polarized and might explain the decrease in the total PD. However, the soft thermal component accounts for just 5–10% of the total emission (7.7% ± 1.4% between 2 and 3 keV, according to the NICER spectral analysis reported in Sect. 3.1.1). As a result, the influence of this unpolarized component at low energies does not readily explain the observed decrease in the PD. The analysis presented in Sect. 3.1.1 shows that to explain the decrease of the total polarization, the soft thermal component should be polarized to a degree of 8% ± 5% and its polarization angle should differ by ~90° from the polarization angle compared to the Comptonization component. However, the improvement in the fit description compared to a model with the same polarization properties for the two spectral components is modest. As thermal unscattered emission is not expected to be polarized, an intrinsic decrease in the polarization degree of the Compton-scattered photons is a more likely explanation of the observed energy dependence. Bobrikova et al. (2023) predicted a swing by ~90° of the polarization vector of the Comptonized emission at an energy of ≃5 keV, which is only slightly higher than the turnover energy of ≃3 keV we observed. A comprehensive analysis of the spectral properties of the source that also includes XMM–Newton data is in preparation.

3.2. X-ray-pulsed variability

3.2.1. Pulse-phase timing solution

We used the pulsar-timing solutions based on the first few days of NICER observations (Ng et al. 2024) to correct the arrival time of X-ray photons for the light travel-time delays due to the pulsar orbit. We used two harmonic components to model the pulse profiles obtained by folding data taken in ~500 s-long intervals and sampled by 16 phase bins. Table 2 shows the timing solutions based on the observed evolution of the phase computed over the fundamental harmonic for the various instruments considered here, plotted in Fig. 5 with the best-fitting linear trend). We attribute the residual random phase-variability by ~0.05–0.1 cycles to pulse-timing noise, as observed from other AMSPs with an even larger magnitude (Patruno & Watts 2021; Di Salvo & Sanna 2022). The two values of the pulse phase measured by NICER at MJD 60 384, after an interruption of the monitoring due to visibility constraints, agree with the trend observed earlier and allow us to place a tight upper limit on the spin frequency derivative ($\dot{\nu} < 1.2 \times 10^{-13}$ Hz s^{-1}). However, we caution that this alignment could be fortuitous, as the pulse phase of AMSPs often shows erratic variability, especially in the late stages of an outburst (see, e.g. Illiano et al. 2023).

We used these ephemerides to fold 5 ks long intervals of IXPE data and recover the pulsed signal despite the lower counting statistics. Figure 6 shows the fractional amplitude and phase of the fundamental harmonic observed by IXPE. An increase in the amplitude from ~4 to 15% is observed after MJD 60 376.5.

The frequencies measured by NuSTAR, IXPE, and XMM–Newton differ by $\delta\nu/\nu \simeq 0.3 \times 10^{-9}$, 0.6×10^{-9}, and 2×10^{-9} with respect to the NICER measurement, respectively. The latter is compatible with the value quoted in the latest calibration technical note for the XMM–Newton clock relative time-accuracy[3] ($\delta\nu/\nu \simeq 10^{-8}$). The pulse phase recorded by NuSTAR and IXPE at epoch T_0 precedes the phases observed by NICER by 0.07–0.1 cycles. The NuSTAR shift can be understood in terms of the dependence of the pulse phase on energy that was noticed by SRG/ART-XC (Molkov et al. 2024); the reason for the IXPE mismatch is less clear and will be addressed in a future paper. For consistency, the phase-resolved analysis presented in Sect. 3.2.2 was based on the IXPE timing solution, even though this is slightly less accurate.

3.2.2. Phase-resolved polarization variability

To perform a phase-resolved analysis of the polarimetric properties of SRGA J1444, we considered IXPE data corrected for the orbital parameters listed in Table 2. We used the `pcube` algorithm to evaluate in $n = 16$ phase bins the Stokes parameters Q and U, which are expected to be normally distributed

---

[3] `https://xmmweb.esac.esa.int/docs/documents/CAL-TN-0018.pdf`

Table 2. Pulse-phase timing solutions of SRGA J1444.

	NICER	XMM–Newton	NuSTAR	IXPE
Interval (MJD)	60 361.837–60 383.544	60 368.106–60 369.374	60 366.465–60 369.881	60 367.615–60 377.619
$\phi(T_0)$	0.47 (1)	0.500 (7)	0.400 (5)	0.37 (1)
$\nu(T_0)$ (Hz)	447.87156112 (2)	447.8715620 (3)	447.87156127 (2)	447.87156138 (8)
$\dot{\nu}$ (Hz s^{-1})	$<1.2 \times 10^{-13}$	$<7.0 \times 10^{-12}$	$<1.5 \times 10^{-12}$	$<3.0 \times 10^{-13}$
$a_1 \sin i/c$ (lt-s)	0.65052 (2)	0.650491 (5)	0.650498 (3)	0.650486 (13)
$P_{\rm orb}$ (s)	18 803.65 (1)	18 803.65 (1)	18 803.673 (4)	18 803.665 (4)
$T_{\rm asc}$ (MJD)	60 361.641306 (3)	60 361.641305 (6)	60 361.641297 (2)	60 361.641310 (5)
e	$<9 \times 10^{-5}$	$<9 \times 10^{-5}$	$<3 \times 10^{-5}$	$<1.0 \times 10^{-4}$
χ^2 (d.o.f.)	93.0 (53)	368.5 (212)	1261.8 (762)	121.3 (53)

Notes. All the solutions presented in the table were obtained by folding the data around $\nu_{\rm fold}$ = 447.87156116029 Hz with a reference epoch MJD 60 361.8. To facilitate the comparison, the frequency estimates were evaluated at T_0 = MJD 60 368.0. All the epochs reported here are in the barycentric dynamical time (TDB) system. Uncertainties at the 1σ c.l. are reported in parentheses. Upper limits are given at a 90% c.l.

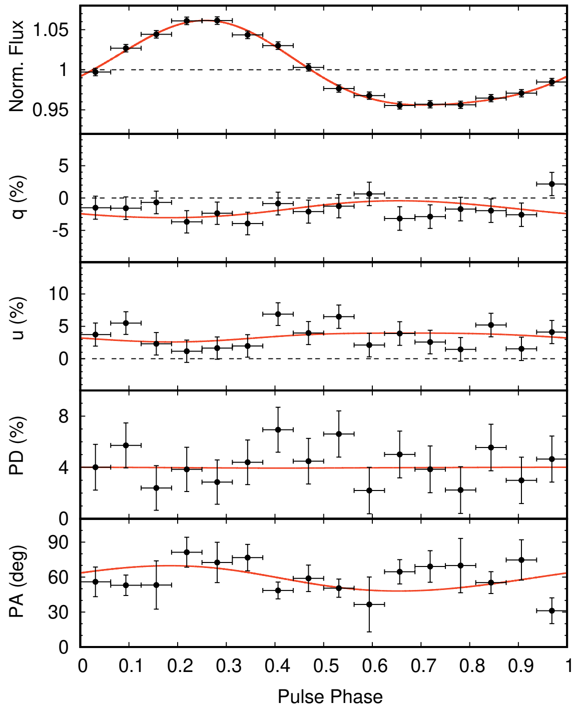

Fig. 7. Pulse-phase dependence of the polarimetric properties. From top to bottom: Total flux normalized to the average, normalized Stokes parameters $q = Q/I$ and $u = U/I$, and the PD and PA observed by IXPE during the interval MJD 60 367.6–60 376.5 as a function of the spin phase. The solid red line indicates the model obtained by fitting the absolute Stokes parameters assuming two point-like spots and the parameters listed in the text.

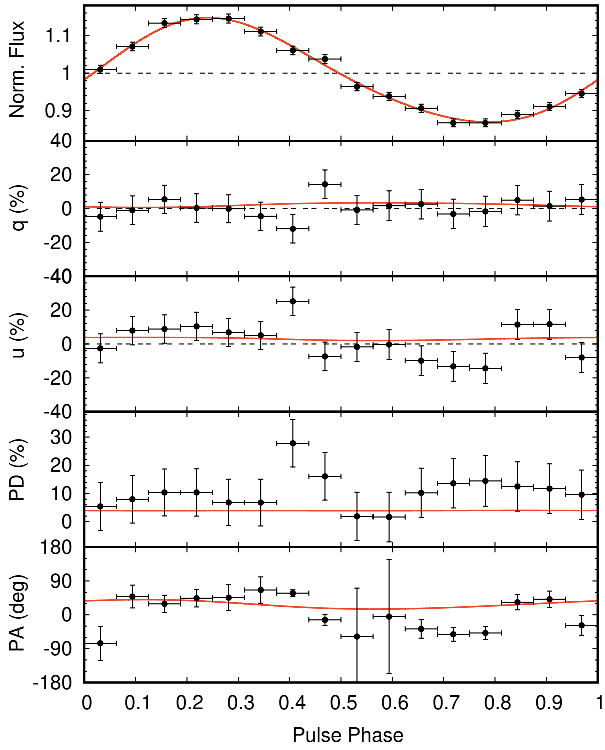

Fig. 8. Same as Fig. 7, but for the interval MJD 60 376.5–60 377.7 only.

(González-Caniulef et al. 2023; Suleimanov et al. 2023). We restricted the analysis to the 3–6 keV energy band in order to maximize the strength of the polarized signal. We used the `pcube` algorithm without acceptance corrections to measure the Stokes parameters in counts per second.

Figure 7 shows the phase-resolved Stokes parameters, the PD, and the PA observed before the pulse amplitude increase that occurred at MJD 60 376.5. The Stokes parameters Q and U did not show significant variability. A fit with a constant function gave a χ^2 of 16.6 and 15.6 for 15 d.o.f., respectively, with average values of $q = Q/I = -1.6\% \pm 0.5\%$ and $u = U/I = 3.5\% \pm 0.4\%$.

We also separately analyzed data taken after the pulse amplitude increase, which occurred at MJD 60 376.5 (see Fig. 8). Fitting with a constant gives $q' = 0.5\% \pm 1.4\%$ and $u' = 2.4\% \pm 2.7\%$ for $\chi^2 = 10.2$ and 18.7 for 15 d.o.f. The two Stokes parameters are compatible with zero within the uncertainties, even though the value of u' measured at phase 0.4 significantly deviated from the trend, leading to an increase in the PD up to ~30%.

We also measured the Stokes parameters over 15 orbital phase bins to search for orbital variability in the polarization properties, but found none that was significant. Constant values of Q and U modeled the dependence of these values on the orbital phase well ($\chi^2 = 9.1$ and 12.5 for 14 d.o.f., respectively).

3.2.3. Modeling the phase-resolved polarization properties

When we assume that the accretion columns are the source of the polarized X-ray photons we observed, it is necessary to ask

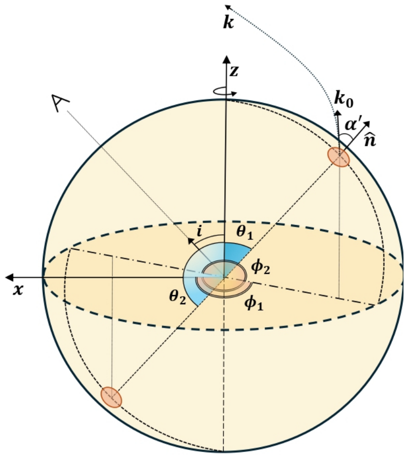

Fig. 9. Assumed geometry of the problem, adapted from Poutanen & Beloborodov (2006). The binary inclination i, the colatitutde of the two spots θ_1 and θ_2, their phases ϕ_1 and ϕ_2, and the angle made by the direction of the emitted photon with respect to the normal to the spot in the comoving frame α' are explicitly indicated.

which geometrical configuration of the spot can simultaneously explain the observed pulse profile and the insignificant phase-resolved variability in the Stokes parameters Q and U.

Unlike the case of highly magnetized slowly rotating X-ray pulsars (Doroshenko et al. 2022; Tsygankov et al. 2022; Mushtukov et al. 2023; Marshall et al. 2022; Forsblom et al. 2023; Tsygankov et al. 2023; Malacaria et al. 2023; Doroshenko et al. 2023; Suleimanov et al. 2023; Poutanen et al. 2024; Forsblom et al. 2024), the polarization properties of AMSPs are defined by the geometry of the spots, relativistic effects (Viironen & Poutanen 2004; Poutanen 2020; Loktev et al. 2020), and possibly eclipses by the inner parts of the accretion disks (Poutanen et al. 2009; Ibragimov & Poutanen 2009). This prevents us from using a simple rotating vector model to fit the observed phase-resolved PD and PA, but requires a fit of the total Stokes vector (I, Q, U), which is the sum of the Stokes vectors of the two spots.

The Stokes parameters of the spots depend on the variation in the total and polarized radiation with the spin phase, photon energy, and zenith angle (Viironen & Poutanen 2004; Poutanen 2020; Salmi et al. 2021; Bobrikova et al. 2023). A modeling that includes an accurate description of all these effects is beyond the scope of this paper and will be presented elsewhere. We considered the system geometry by using the approximate formulae given by Poutanen & Beloborodov (2006) and Poutanen (2020) for the phase-resolved Stokes parameters. We assumed two point-like spots on the surface of a fast-rotating NS (see Fig. 9 for a cartoon of the assumed geometry) that emit X-rays with a power-law spectrum with $I(\alpha', E) = I_0(1 + h\cos\alpha')E^{-(\Gamma-1)}$. Here, $\Gamma = 1.7$ is the spectral photon index, α' is the zenith angle (i.e., the angle between the normal to the spot and emission direction) in the corotating frame, and h is an anisotropy parameter ($h = 0$ for blackbody emission, and $-1 < h < 0$ for a fan-beam pattern such as is expected from Comptonization in a thin slab; Poutanen & Gierliński 2003). We used Eqs. ((20)–(22)) of Poutanen & Beloborodov (2006) to determine the phase intervals in which the photons are visible to the observer and Eqs. ((28)–(34)) of the same paper to express the flux observed from each spot, $F_i(\phi_i + \phi_0, i, \theta_i, h)$ $(i = 1, 2)$ at a given binary inclination i and colatitude θ_i of the spot, and the resulting total flux $F_{\rm tot}(\phi) = N(F_1 + F_2)$. Here, N is a normalization constant, ϕ_0 is the spin phase of the primary spot at the folding reference epoch. We assumed the phase of the secondary spot to be $\phi_2 = \phi_1 + \pi$ and used the relativistic rotating-vector model of Poutanen (2020) to express the phase-resolved Stokes parameters of each of the two spots (Eqs. (58) and (59)), assuming that NF_i gives the observed flux and that their polarization degree $p_1 = p_2$ does not depend on energy and zenith angle. We then used (Eqs. (21)–(23)) of the same paper to compute the total expected Stokes vector, $Q = Q_1 + Q_2$ and $U = U_1 + U_2$.

We fit the phase-resolved Stokes parameters observed before the amplitude increase (see Fig. 7) with our simple model and fixed the NS mass and radius to $M = 1.4\,M_\odot$ and $R_{\rm eq} = 10$ km as the fit was insensitive to the choice of these parameters within a range of reasonable values for an NS. The fit (see Fig. 7) suggests a configuration with two visible spots as the fit χ^2 (38.8 for 41 d.o.f.) improves compared to a fit with only one spot ($\chi^2 = 63.0$ for 42 d.o.f.; the probability of a chance improvement is $\simeq 10^{-5}$ according to an F-test). A reasonably good fit can be obtained for any value of h ranging between 0 and -1. We show the results obtained for a randomly chosen intermediate value of $h = -0.3$. We find a best fit for $i = (74.1^{+5.8}_{-6.3})^\circ$, $\theta_1 = (11.8^{+2.5}_{-3.5})^\circ$, $\theta_2 = (172.6^{+2.0}_{-1.0})^\circ$, $\phi_0 = 0.57(4)$, $N = 6.90(6) \times 10^4$ cnt, $p_1 = 4.0\% \pm 2.0\%$ and $\chi_{\rm p} = 57\overset{\circ}{.}2 \pm 0\overset{\circ}{.}5$, where the latter is the position angle of the angular pulsar momentum. We evaluated uncertainties at the 1σ c.l. from the variation in the fit χ^2 for the number of interesting parameters measured ($\Delta\chi^2 = 8.15$ for 7 parameters Lampton et al. 1976). These uncertainties have to be taken with caution, as they were obtained for fixed values of the NS mass, radius, and emission anisotropy parameter. In addition, the strong correlation between the parameters warrants a study of the posterior distribution of the parameters that were fit using the likelihood function for I, Q, and U, which will be presented in a forthcoming paper. The red line in Fig. 7 marks the predicted model of the normalized Stokes parameters obtained for these parameters. The bottom panels of the same figure show the total PD $= \sqrt{q^2 + u^2}$ and PA $= \chi_{\rm p} + \frac{1}{2}\tan^{-1}(u/q)$, respectively. The absence of significant variability with the pulse phase of the phase-resolved observed normalized Stokes parameters q and u can be explained by two almost antipodal spots if their magnetic inclination is low. The observed roughly constant phase-resolved trend gives little information on the other parameters, however, which are essentially set by the total pulse profile alone. Molkov et al. (2024) used a modeling similar to ours (even though they assumed extended spots) and found qualitatively similar results ($i = 58^\circ$ and $\theta_1 = 14^\circ$, $\theta_2 = \pi - \theta_1$). They modeled a pulse with a higher amplitude (9–12%) than ours ($A_1 = 5.2\% \pm 0.1\%$) and a plateau close to the pulse minimum, which they interpreted in terms of occultation by the inner accretion disk extending down to ~25 km. The flattening of the pulse profile observed by IXPE is less pronounced, and no partial occultation is required for a qualitative modeling of the profile. Because the pulse profile Molkov et al. (2024) modeled was observed when the X-ray flux was roughly double that observed by IXPE, this might indicate a recession of the inner accretion disk at a decreasing mass-accretion rate.

After MJD 60 376.5, the pulsed fraction observed by IXPE increased to $A_1 = 18.7\% \pm 0.8\%$ (see Fig. 6). The same model as described above with the binary inclination and the anisotropy parameter fixed to $i = 74\overset{\circ}{.}1$ and $h = -0.3$, respectively, provides a good fit of the profile observed after this epoch, with a spot magnetic inclination and longitude increased by $\simeq 10^\circ$ and ~20°, respectively, and a polarization degree decreased to $2.0\% \pm 1.5\%$ compared to the observations performed previously. The observed change in the pulse-profile shape could then reflect motions of the hot spots, as is often assumed to explain the timing noise observed from AMSPs (see, e.g., Lamb et al. 2009). The profile predicted using our model is plotted as a red line in Fig. 8.

4. Type I X-ray bursts

During the observations reported here, IXPE detected 52 type-I X-ray bursts that shared similar properties (see the inset of Fig. 10 for an example). The sample of peak count rates had an average of 38.7 cnt $\mathrm{s^{-1}}$ and a standard deviation of 2.9 cnt $\mathrm{s^{-1}}$. After subtracting the persistent emission, the distribution of the fluence of the observed bursts had an average of 649 cnt with a standard deviation of 40; the fluence of the different bursts was very similar and only slightly increased for bursts that occurred when the persistent count rate had decreased below 3 cnt $\mathrm{s^{-1}}$. The relatively low number of counts observed by IXPE prevented us from performing a time-resolved spectral analysis of the single bursts. By stacking all the observed bursts and fitting the observed spectra with the sum of a thermal component and the two-component model used to fit the persistent spectrum (see Sect. 3.1.1), we obtained $\langle kT_{\rm burst}\rangle = 1.83 \pm 0.05$ keV and $R_{\rm burst} = (6.2 \pm 0.2)d_8$ km. Defining the burst duration as $\tau = \mathcal{F}/F_{\rm peak}$ and neglecting variations of the spectrum throughout the burst, we obtained $\tau = 16.8 \pm 1.6$ s. Figure 10 shows the recurrence times $\Delta t_{\rm rec}$ between the observed bursts[4] as a function of the average persistent count rate C measured during the longest possible contiguous interval before the burst. For 14 bursts, we scaled the time that elapsed since the previous burst by a factor of 2 as the immediately preceding burst was likely missed due to interruption in the IXPE coverage (green points in Fig. 10). For one burst (red point), we used a scaling factor of 3.

4.1. X-ray polarimetry of the burst emission

To search for a polarized signal during the X-ray bursts, we stacked the emission observed during all the events, retaining 32 s after the onset of each of the bursts for a total exposure of 1664 s. We measured $q_{\rm b} = Q_{\rm b}/I_{\rm b} = -0.8\% \pm 3.3\%$ and $u_{\rm b} = U_{\rm b}/I_{\rm b} = 2.8\% \pm 3.3\%$, resulting in an upper limit on the PD of the sum of the burst and the persistent emission of $\mathrm{PD_{UL}} = 7.2\%$ (90% c.l.). We then subtracted the absolute Stokes vectors observed during the persistent emission after normalizing them to the exposure time of 1664 s over which the burst emission was integrated, summing in quadrature the uncertainties, and obtained normalized Stokes parameters $\tilde{q}_{\rm b} = -0.7\% \pm 3.9\%$ and $\tilde{u}_{\rm b} = 3.0\% \pm 3.9\%$, corresponding to an upper limit on the PD of the burst emission of 8.5% (90% c.l.).

4.2. Implications

To our knowledge, the observations presented here are the first in which IXPE caught thermonuclear X-ray bursts from an accreting NS. The ~10 d coverage of the outburst of SRGA J1444 allowed us to detect 52 bursts and stack them when we searched for a polarized signal. The upper limit we placed on the PD of the burst emission (8.5%) is higher than the maximum value estimated by Lapidus & Sunyaev (1985) assuming reflection of the burst emission by the accretion disk (3.7% for an inclination of 72°). With a recurrence time that varies between ≃1.6 h at the beginning of the outburst (Molkov et al. 2024) and ≃8 h at the end of the IXPE observation presented here, SRGA J1444 was immediately recognized as a very prolific burster. The 11 Hz pulsar IGR J17480–2446 (which showed a decreasing recurrence time from ≃30 to ≃3 minutes; Motta et al. 2011; Chakraborty et al. 2011; Linares et al. 2012) and 4U 1636–536 (with a recurrence time of ≃30 minutes and even less energetic short-recurrence time bursts; Beri et al. 2019) are similar cases. Among accreting MSPs, SAX J17498–2021 showed bursts between 1 and 2 h (Li et al. 2018), IGR J17511–3057 between 7 and 21 h (Falanga et al. 2011) and IGR J17498–2921 every 16–18 h (Falanga et al. 2012), in all cases with a recurrence time that increased as the X-ray flux declined. The ≃17 s duration of the bursts seen from SRGA J1444 suggests that they ignite in a mixed H/He environment. The hot CNO cycle is expected to deplete the accreted hydrogen in $9.8(X/0.7)(Z/0.02)^{-1}$ h, where H and Z are the hydrogen and metal abundances (see Galloway et al. 2022, and references therein). The range of observed recurrence times (<8 h) suggests that a complete depletion of hydrogen could only be achieved if the H abundance were subsolar. For bursts igniting in a mixed H/He environment, the burst ignition depth is not expected to depend much on the mass-accretion rate $\dot{M}$ and the recurrence timescale should increase as $\Delta t \propto \dot{M}^{-1}$. When we assume that the IXPE count rate is a good tracer of the mass accretion rate, the observed dependence (see Fig. 10) is broadly compatible with this expectation.

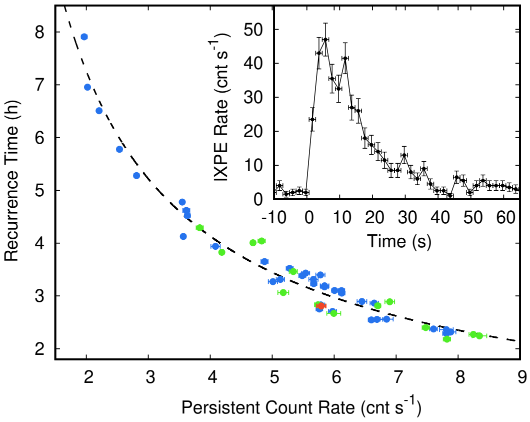

Fig. 10. Recurrence time of the type-I X-ray bursts observed by IXPE evaluated as the interval between consecutive bursts scaled by a factor of 1 (blue points), 2 (green), and 3 (red) as a function of the persistent count rate observed before the burst C. The dashed line shows the relation $\Delta t_{\rm rec} = KC^{-0.8}$ with $K = 12.75$ h. The inset shows the profile of the burst observed starting at MJD 60 377.05969.

5. Conclusions

We presented the first X-ray polarimetric IXPE observation of an accreting millisecond pulsar in outburst, SRGA J1444, in the context of an observational campaign that also involved NICER, NuSTAR, and XMM-Newton observations. The main results are listed below.

- The 2–8 keV emission is significantly polarized, with an average degree of 2.3% ± 0.4% at an angle of 59° ± 6° (east of north).
- We observed a significant change in the polarization properties with energy. The PD is maximum between 3 and 6 keV (4.0% ± 0.5%) and decreases to <2% (90% c.l.) in the 2–3 keV range.
- The pulse phase of SRGA J1444 is rather stable throughout the observations presented here, with an upper limit on the

---

[4] Consecutive bursts without data gaps could not be observed in IXPE data, but the uninterrupted XMM coverage allowed us to define the recurrence time unambiguously.

spin-frequency derivative of $\dot{\nu} < 1.2 \times 10^{-13}$ Hz s^{-1}. During the IXPE observations, the pulse had an amplitude of ~5% before it abruptly increased to almost 20% roughly one day before the end of the coverage.

- The observed phase-resolved Stokes parameters are compatible with a constant function. A simple approximate model of the Stokes vector expected from the sum of two almost antipodal spots on the NS surface reproduced the observed values for a binary inclination of $i = (74.1^{+5.8}_{-6.3})^{\circ}$ and relatively low magnetic inclination of the spots $\theta_1 = (11.8^{+2.5}_{-3.5})^{\circ}$, $\theta_2 = (172.6^{+2.0}_{-1.0})^{\circ}$. The little phase-resolved variability shown by the Stokes parameters, if any, prevented us from obtaining constraints on the NS mass and radius based on our simple modeling.
- IXPE observed 52 type I X-ray bursts with similar properties (e.g. burst peak fluence, duration, and fluence) with a recurrence time that increased as a function of the observed count rate, $\Delta t_{\rm rec} \propto C^{-0.8}$. After we subtracted the persistent emission, the upper limit on the PD observed in the stacked burst emission was 8.5% (90% c.l.).

The first significant detection of polarization from an accreting millisecond pulsar confirms theoretical expectations and strengthens the prospects of using this technique to measure the geometrical parameters of accreting MSPs and obtain constraints on the mass and radius of the NS from pulse-profile modeling. Future IXPE observations of accreting millisecond pulsar outbursts will hopefully detect a larger phase-resolved variability and enable a more accurate determination than those allowed by the current dataset.

Acknowledgements. We warmly thank the Directors and the Science Operations Team of IXPE, NICER, NuSTAR, and XMM for promptly scheduling the observations reported here and Bas Dorsman, Matteo Bachetti and Anna Watts for useful discussions. The Imaging X-ray Polarimetry Explorer (IXPE) is a joint US and Italian mission. The US contribution is supported by the National Aeronautics and Space Administration (NASA) and led and managed by its Marshall Space Flight Center (MSFC), with industry partner Ball Aerospace (contract NNM15AA18C). The Italian contribution is supported by the Italian Space Agency (Agenzia Spaziale Italiana, ASI) through contract ASI-OHBI-2022-13-I.0, agreements ASI-INAF-2022-19-HH.0 and ASI-INFN-2017.13-H0, and its Space Science Data Center (SSDC) with agreements ASI-INAF-2022-14-HH.0 and ASI-INFN 2021-43-HH.0, and by the Istituto Nazionale di Astrofisica (INAF) and the Istituto Nazionale di Fisica Nucleare (INFN) in Italy. This research used data products provided by the IXPE Team (MSFC, SSDC, INAF, and INFN) and distributed with additional software tools by the High-Energy Astrophysics Science Archive Research Center (HEASARC), at NASA Goddard Space Flight Center (GSFC). NICER is a 0.2–12 keV X-ray telescope operating on the International Space Station, funded by NASA. The NuSTAR mission is a project led by the California Institute of Technology, managed by the Jet Propulsion Laboratory, and funded by the National Aeronautics and Space Administration. Data analysis was performed using the NuSTAR Data Analysis Software (NuSTARDAS), jointly developed by the ASI Science Data Center (SSDC, Italy) and the California Institute of Technology (USA). XMM-Newton is an ESA science mission with instruments and contributions directly funded by ESA Member States and NASA. MN and this work were supported by NASA under grant 80NSSC24K1175. AP, GI, FA, RLP, CM and LS are supported by INAF Research Grant FANS and the Italian Ministry of University and Research PRIN 2020 Grant 2020BRP57Z (GEMS). AP acknowledges support from the Fondazione Cariplo/CDP, grant no. 2023-2560. JP thanks the Ministry of Science and Higher Education grant 075-15-2024-647 for support. AB acknowledges support from the Finnish Cultural Foundation grant 00240328. MCB acknowledges support from the INAF-Astrofit fellowship. FCZ is supported by a Ramón y Cajal fellowship (grant agreement RYC2021-030888-I). TS acknowledges support from ERC Consolidator Grant No. 865768 AEONS (PI: Watts).

References

Baglio, M. C., Russell, D. M., Saikia, P., et al. 2024, ATel, 16487, 1
Baldini, L., Bucciantini, N., Di Lalla, N., et al. 2022, SoftwareX, 19, 101194
Baym, G., Hatsuda, T., Kojo, T., et al. 2018, Rep. Progr. Phys., 81, 056902
Beri, A., Paul, B., Yadav, J. S., et al. 2019, MNRAS, 482, 4397
Bobrikova, A., Loktev, V., Salmi, T., & Poutanen, J. 2023, A&A, 678, A99
Chakraborty, M., Bhattacharyya, S., & Mukherjee, A. 2011, MNRAS, 418, 490
Choudhury, D., Salmi, T., Vinciguerra, S., et al. 2024, ApJ, 971, L20
Di Marco, A., Costa, E., Muleri, F., et al. 2022, AJ, 163, 170
Di Marco, A., Soffitta, P., Costa, E., et al. 2023, AJ, 165, 143
Di Salvo, T., & Sanna, A. 2022, ASSL, 465, 87
Dittmann, A. J., Miller, M. C., Lamb, F. K., et al. 2024, ApJ, 974, 295
Doroshenko, V. 2024, A&A, submitted [arXiv:2403.03127]
Doroshenko, V., Poutanen, J., Tsygankov, S. S., et al. 2022, Nat. Astron., 6, 1433
Doroshenko, V., Poutanen, J., Heyl, J., et al. 2023, A&A, 677, A57
Falanga, M., Kuiper, L., Poutanen, J., et al. 2011, A&A, 529, A68
Falanga, M., Kuiper, L., Poutanen, J., et al. 2012, A&A, 545, A26
Forsblom, S. V., Poutanen, J., Tsygankov, S. S., et al. 2023, ApJ, 947, L20
Forsblom, S. V., Tsygankov, S. S., Poutanen, J., et al. 2024, A&A, 691, A216
Galloway, D. K., Johnston, Z., Goodwin, A., & He, C.-C. 2022, ApJS, 263, 30
González-Caniulef, D., Caiazzo, I., & Heyl, J. 2023, MNRAS, 519, 5902
Ibragimov, A., & Poutanen, J. 2009, MNRAS, 400, 492
Illiano, G., Papitto, A., Sanna, A., et al. 2023, ApJ, 942, L40
Illiano, G., Coti Zelati, F., Marino, A., et al. 2024, ATel, 16510, 1
Kislat, F., Clark, B., Beilicke, M., & Krawczynski, H. 2015, Astropart. Phys., 68, 45
Lamb, F. K., Boutloukos, S., Van Wassenhove, S., et al. 2009, ApJ, 706, 417
Lampton, M., Margon, B., & Bowyer, S. 1976, ApJ, 208, 177
Lapidus, I. I., & Sunyaev, R. A. 1985, MNRAS, 217, 291
Lattimer, J. M., & Prakash, M. 2016, Phys. Rep., 621, 127
Li, Z., De Falco, V., Falanga, M., et al. 2018, A&A, 620, A114
Lightman, A. P., & Zdziarski, A. A. 1987, ApJ, 319, 643
Linares, M., Altamirano, D., Chakrabarty, D., Cumming, A., & Keek, L. 2012, ApJ, 748, 82
Lo, K. H., Miller, M. C., Bhattacharyya, S., & Lamb, F. K. 2013, ApJ, 776, 19
Loktev, V., Salmi, T., Nättilä, J., & Poutanen, J. 2020, A&A, 643, A84
Malacaria, C., Heyl, J., Doroshenko, V., et al. 2023, A&A, 675, A29
Mariani, I., Motta, S., Baglio, M. C., et al. 2024, ATel, 16475, 1
Marshall, H. L., Ng, M., Rogantini, D., et al. 2022, ApJ, 940, 70
Matsuoka, M., Kawasaki, K., Ueno, S., et al. 2009, PASJ, 61, 999
Meszaros, P., Novick, R., Szentgyorgyi, A., Chanan, G. A., & Weisskopf, M. C. 1988, ApJ, 324, 1056
Miller, M. C., & Lamb, F. K. 2015, ApJ, 808, 31
Miller, M. C., & Lamb, F. K. 2016, Eur. Phys. J. A, 52, 63
Miller, M. C., Lamb, F. K., Dittmann, A. J., et al. 2019, ApJ, 887, L24
Miller, M. C., Lamb, F. K., Dittmann, A. J., et al. 2021, ApJ, 918, L28
Molkov, S. V., Lutovinov, A. A., Tsygankov, S. S., et al. 2024, A&A, 690, A353
Morsink, S. M., & Leahy, D. A. 2011, ApJ, 726, 56
Motta, S., D'Aì, A., Papitto, A., et al. 2011, MNRAS, 414, 1508
Mushtukov, A. A., Tsygankov, S. S., Poutanen, J., et al. 2023, MNRAS, 524, 2004
Nagirner, D. I., & Poutanen, J. 1993, A&A, 275, 325
Nagirner, D. I., & Poutanen, J. 1994, Astrophys. Space. Phys. Rev., 9, 1
Ng, M., Ray, P. S., Sanna, A., et al. 2024, ApJ, 968, L7
Özel, F., & Freire, P. 2016, ARA&A, 54, 401
Patruno, A., & Watts, A. L. 2021, ASSL, 461, 143
Poutanen, J. 2006, Adv. Space Res., 38, 2697
Poutanen, J. 2020, A&A, 641, A166
Poutanen, J., & Beloborodov, A. M. 2006, MNRAS, 373, 836
Poutanen, J., & Gierliński, M. 2003, MNRAS, 343, 1301
Poutanen, J., & Svensson, R. 1996, ApJ, 470, 249
Poutanen, J., Ibragimov, A., & Annala, M. 2009, ApJ, 706, L129
Poutanen, J., Tsygankov, S. S., Doroshenko, V., et al. 2024, A&A, 691, A123
Radhakrishnan, V., & Cooke, D. J. 1969, Astrophys. Lett., 3, 225
Riley, T. E., Watts, A. L., Bogdanov, S., et al. 2019, ApJ, 887, L21
Riley, T. E., Watts, A. L., Ray, P. S., et al. 2021, ApJ, 918, L27
Russell, T. D., Carotenuto, F., van den Eijnden, J., et al. 2024, ATel, 16511, 1
Salmi, T., Nättilä, J., & Poutanen, J. 2018, A&A, 618, A161
Salmi, T., Loktev, V., Korsman, K., et al. 2021, A&A, 646, A23
Salmi, T., Choudhury, D., Kini, Y., et al. 2024, ApJ, 974, 294
Suleimanov, V. F., Forsblom, S. V., Tsygankov, S. S., et al. 2023, A&A, 678, A119
Tsygankov, S. S., Doroshenko, V., Poutanen, J., et al. 2022, ApJ, 941, L14
Tsygankov, S. S., Doroshenko, V., Mushtukov, A. A., et al. 2023, A&A, 675, A48
Viironen, K., & Poutanen, J. 2004, A&A, 426, 985
Vinciguerra, S., Salmi, T., Watts, A. L., et al. 2024, ApJ, 961, 62
Watts, A. L., Andersson, N., Chakrabarty, D., et al. 2016, Rev. Mod. Phys., 88, 021001
Weisskopf, M. C., Soffitta, P., Baldini, L., et al. 2022, JATIS, 8, 026002
Wilms, J., Allen, A., & McCray, R. 2000, ApJ, 542, 914